



Original paper

## Spinning slithole collimation for high-sensitivity small animal SPECT: Design and assessment using GATE simulation



Hojjat Mahani<sup>a,b</sup>, Gholamreza Raisali<sup>a</sup>, Alireza Kamali-Asl<sup>c</sup>, Mohammad Reza Ay<sup>b,d,\*</sup>

<sup>a</sup> Radiation Application Research School, Nuclear Science and Technology Research Institute, Tehran, Iran

<sup>b</sup> Research Center for Molecular and Cellular Imaging, Tehran University of Medical Science, Tehran, Iran

<sup>c</sup> Radiation Medicine Department, Shahid Beheshti University, Tehran, Iran

<sup>d</sup> Department of Medical Physics and Biomedical Engineering, Tehran University of Medical Science, Tehran, Iran

### ARTICLE INFO

#### Article history:

Received 7 March 2017

Received in Revised form 16 June 2017

Accepted 6 July 2017

Available online 13 July 2017

#### Keywords:

Slithole collimator

Sensitivity

Molecular SPECT

Planar projections

GATE

### ABSTRACT

**Purpose:** While traditional collimations are widely used in preclinical SPECT imaging, they usually suffer from possessing a low system sensitivity leading to noisy images. In this study, we are aiming at introducing a novel collimator, the slithole, offering a superior resolution-sensitivity tradeoff for small animal SPECT.

**Methods:** The collimator was designed for a molecular SPECT scanner, the HiReSPECT. The slithole is a knife-edge narrow long aperture extended across long-axis of the camera's head. To meet the data completeness requirement, the collimator-detector assembly spins at each regular SPECT angle. The collimator was modeled within GATE Monte Carlo simulator and the data acquisition was performed for NEMA Image Quality (IQ) phantom. In addition, a dedicated 3D iterative reconstruction algorithm based upon plane-integral projections was also developed.

**Results:** The mean sensitivity of the slithole is 285 cps/MBq while the current parallel-hole collimator holds a sensitivity of 36 cps/MBq at a 30 mm distance. The slithole collimation gives rise to a tomographic resolution of 1.8 mm compared to a spatial resolution of  $\sim 1.7$  mm for the parallel-hole one (even after resolution modeling). A 1.75 reduction factor in the noise level was observed when the current parallel-hole collimator is replaced by the slithole. Furthermore, quantitative analysis proves that 3 full-iterations of our dedicated image reconstruction lead to optimal image quality. For the largest rod in the NEMA IQ phantom, a recovery coefficient of  $\sim 0.83$  was obtained.

**Conclusion:** The slithole collimator outperforms the current parallel-hole collimation by exhibiting a better resolution-sensitivity compromise for preclinical SPECT studies.

© 2017 Associazione Italiana di Fisica Medica. Published by Elsevier Ltd. All rights reserved.

## 1. Introduction

SPECT scanner design is always challenged by the well-known resolution-sensitivity relationship [1]. In other words, spatial resolution of a SPECT scan improves at the cost of a reduction in sensitivity. In molecular SPECT, the problem is more challenging since the use of high-resolution collimators automatically trades the spatial resolution off against the detection efficiency [2–6]. Therefore, the need for simultaneous high-resolution high-sensitivity SPECT systems mandates to design novel collimation systems exhibiting a different resolution-sensitivity compromise [7–10]. Dynamic cardiac/pulmonary SPECT imaging, low-dose examinations, motion artifact-free scans, and tracer kinetic analysis by

parametric image reconstruction in small animal studies require such a high-resolution high-sensitivity camera.

Several SPECT prototypes have been designed and introduced with a high-sensitivity based on planar projections using rotating slat collimators for clinical studies [11–21] with comparable performance with conventional parallel-hole collimators in terms of spatial resolution and lesion detectability, but with much higher detection efficiency. More specifically, Lodge et al. [16], as pioneers of this field of study, gained 12–28 times greater detection efficiency while maintaining spatial resolution (1.6 cm). Early scanners [10–18] utilized a filtered backprojection (FBP) technique for image reconstruction. Due to noise amplification nature of the FBP methods and their produced streak artifact, a set of fully 3D maximum-likelihood expectation-maximization (MLEM) family iterative reconstruction algorithms have been introduced [20,21]. Complexity of these fully 3D reconstruction methods along with their computation expense of system matrix derivation are still

\* Corresponding author at: Department of Medical Physics and Biomedical Engineering, Tehran University of Medical Sciences, Tehran, Iran.

E-mail address: [mohammadreza\\_ay@sina.tums.ac.ir](mailto:mohammadreza_ay@sina.tums.ac.ir) (M.R. Ay).

challenging problems [21]. Translation of the rotating parallel-slat collimators from clinical researches into preclinical studies was also promising [22,23]. An alternative to the parallel-slat collimators in small animal SPECT scanning, is slit collimation. The concept of slit collimation was initially implemented to a preclinical scanner equipped with solid-state strip detector and utilizing analytic image reconstruction methods [24]. Though, the slit collimator's performance was encouraging, but it is hampered by lack of both a fast high-quality iterative reconstruction algorithm and in-detail collimator modeling and imaging physics during simulations [24].

In this work, a novel simultaneous high-resolution high-sensitivity collimator, called the slithole, is designed for the HiReSPECT – a high-resolution small animal SPECT scanner [25–30]. As the slithole deals with plane-integral data (rather than line-integral data in traditional collimators), it requires a sophisticated data acquisition strategy as well as a dedicated image reconstruction algorithm. The present work is first directed towards the optimal design of the slithole and then to assess its performance using various phantom reconstructions utilizing an in-house fast MLEM-based [31] algorithm. Finally, a fair comparison with the current parallel-hole collimator is made considering the same acquisition time.

**2. Materials and methods**

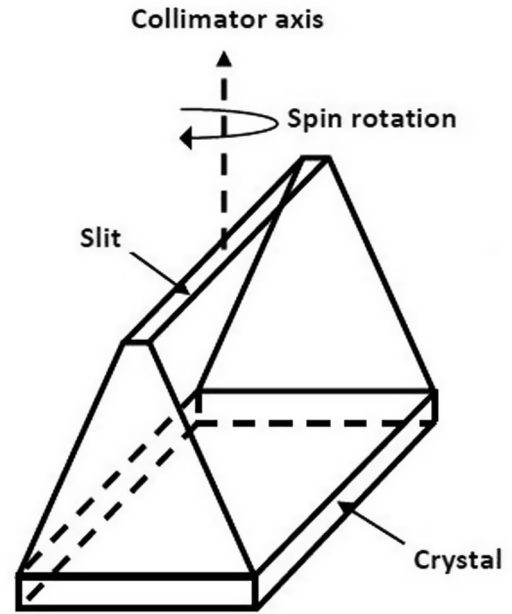
**2.1. The HiReSPECT camera**

The HiReSPECT scanner is a two-headed high-resolution SPECT camera, equipped with a low-energy high-resolution (LEHR) lead parallel-hole collimator (1.2 mm hexagonal holes, 34 mm length, and 0.2 mm septal thickness), a 2D pixelated CsI(Na) crystal (1 × 1 mm<sup>2</sup> pixel area and 0.2 mm Epoxy gap) as well as two position-sensitive photomultiplier tubes (PSPMTs). Field-of-view (FOV) of the camera is 50 mm × 100 mm. Fig. 1 illustrates the camera and some of its key components.

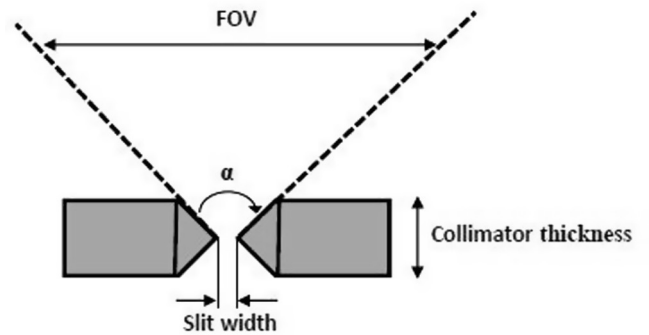
The gantry of the HiReSPECT camera routinely rotates around 180° with 32 stops (total 64 projections over 360°). Imaging time at each stop is 60 s. The SPECT images are iteratively reconstructed using a standard rotation-based resolution-modeled ordered-subset expectation-maximization (OSEM) algorithm [28]. It should be highlighted that the HiReSPECT scanner is capable of rotating each head about their 3own axis, allowing the so-called spin rotation.

**2.2. The slithole**

A 3D schematic view of the slithole collimator is shown in Fig. 2. The slithole is a dual knife-edge aperture embedded in a tungsten



(a)



(b)

**Fig. 2.** (a) A 3D schematic view of the spinning slithole collimator, (b) the slithole's edge.

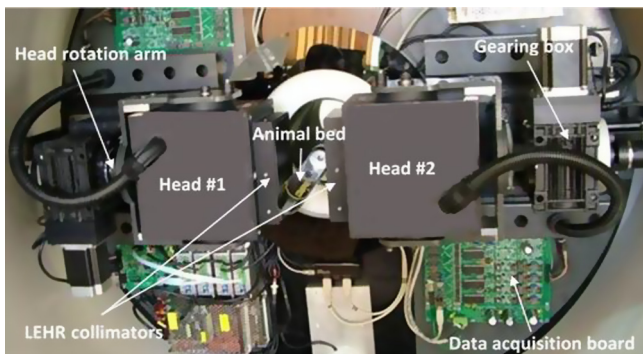


**Fig. 1.** A close-up view of the HiReSPECT scanner. The HiReSPECT is a dual-headed gamma camera designed for molecular SPECT.

**Table 1**  
The characteristics of the slithole collimation used for the HiReSPECT camera.

Parameter	Specification
Slit width	0.6 mm
Focal length	45 mm
Opening angle ( $\alpha$ )	58°
Edge type	Knife-edge
Material	Tungsten
Thickness	2.5 mm
Common FOV	~35 mm at 30 mm ROR

body. Table 1 gives geometry specifications of the slithole. Inherent to the geometry of the slithole, it accepts much more photons and therefore can potentially offer a higher detection efficiency than a parallel-hole collimator can. To guarantee a sufficient measurement of the tomographic data, the collimator-detector pair has to

spin at each regular SPECT angle [11–13] in either a continuous or a step-and-shoot manner. The latter is the data acquisition method of choice.

This collimation system is specifically designed for the HiReSPECT scanner. In other words, one needs only to replace the current parallel-hole collimator with the slithole collimator without any change or modification in the system configuration. Mechanical limitations were also taken into consideration as well. The slithole specifications, tabulated in Table 1, result in a  $\sim 35$  mm FOV at 30 mm radius-of-rotation (ROR) with a magnification factor of 1.5.

### 2.3. Accurate GATE Monte Carlo simulation

MC modeling plays a crucial role in the development of new imaging instrumentation, image acquisition strategies and processing, and reconstruction methods [32,33]. GATE is a dedicated MC simulator optimized for simulations in emission tomography [34,35] and uses well-validated GEANT4 libraries. We first modeled the HiReSPECT scanner with its current configuration and then proceeded to simulate the slithole collimated HiReSPECT camera within the GATE.

To ensure an accurate GATE MC simulation, physics of the imaging process was carefully taken into account in our modeling. Intrinsic spatial (1.2 mm) and energy resolution ( $\sim 20\%$  at 140 keV), dead-time of the CsI(Na) as well as half-life of the  $^{99m}\text{Tc}$  tracer were considered. Two glass PSPMTs were also modeled as backscattering media behind the pixelated crystal. Photoelectric effect, Compton scattering, electron ionization, and multiple-scattering were included as particle interactions. To speed-up the GATE MC simulations, time-consuming transportation of secondary electrons in both the collimator and the phantom was ignored. Detailed tracking of the secondary particles (here, electrons) within both the collimator and the phantom dramatically increases computation burden needed to simulate a SPECT camera, while it adds no useful imaging information. It should be noted that this strategy was not applied to the CsI(Na) crystal, and therefore these secondary electrons were fully tracked within it [29].

### 2.4. Dedicated image reconstruction

To correct the data for Compton scattering, a dual-window based correction method was used [36]. Therefore, two complete datasets at two energy windows were collected. Then, the planar projections were corrected pixel-by-pixel as follows

$$P_{corrected} = P_{photopeak} - k \left( S \times \frac{W_{photopeak}}{W_{scatter}} \right). \quad (1)$$

where  $P_{corrected}$ ,  $P_{photopeak}$ , and  $S$  respectively represent the 1D scatter-corrected planar projection data, the 1D planar projections obtained from the photopeak window, and the scatter planar projection.  $k$  is the calibration factor (here, 0.5),  $W_{photopeak}$  is the width of the photopeak window (here, 28 keV at centered 140 keV), and  $W_{scatter}$  is the width of the scatter window (here, 10 keV centered at 120 keV).

As the slithole collimation data are inherently weighted 3D Radon transform (planar integrals) of the object being imaged [24], we used a 3D sensitivity map (an  $11 \times 11 \times 11$  grid size, 10 mm spacing) covering the entire FOV of the collimator, to compensate planar measurements for location-dependent sensitivity weighting during image reconstruction. This 3D sensitivity map was determined using multiple point source simulations using the GATE, and then normalized to its maximum value within the 3D grid.

Given the special geometry and the imaging protocol of the slithole collimation, an innovative OSEM algorithm was developed.

Prior to reconstructing the images, the emission data were also corrected for Compton scattering as described in the previous subsection. To form 1D planar projections, the 2D acquired data matrix (at each spin angle) were reduced to a 1D vector by summing counts of all crystal pixels in a column parallel to the slit aperture. A 3D matrix representation, called spinogram, is then created with dimensions corresponding to 1D planar projection bins, spin angles, and SPECT angles.

A sensitivity map-incorporated joint rotation-based/plane-driven projector/backprojector pair was introduced. Our fully 3D OSEM reconstruction framework works by: (1) starting with an initial image estimate (commonly a matrix of unity), (2) modeling the sensitivity by voxel-by-voxel multiplying the image volume with the 3D sensitivity map, (3) calculating planar projections, forward projecting, (for SPECT angle  $0^\circ$  and spin angle  $0^\circ$ ) using a plane tracing method in which contribution of each image voxel in a planar projection is weighted by plane-area intersection over that voxel (so the algorithm is plane-driven), (4) rotating the image matrix according to the appropriate spin angle, then forward projecting using step 3 (so the algorithm is rotation-based, for the spin rotation), (5) comparing the calculated planar projections with those of the GATE-provided, and calculating the ratio between them as for an standard MLEM algorithm, (6) backward projecting the ratios into the image volume using the joint rotation-based/plane-driven method, (7) repeating steps 2–6 for all SPECT angles by rotating the image volume according to the appropriate SPECT angles (so the algorithm is also rotation-based, for the SPECT rotation), and (8) repeating steps 2–7 for all full-iterations. Our reconstruction technique is OSEM variant of a standard MLEM algorithm with 16 subsets. It means that the algorithm updates the image once per SPECT view.

To convert the image voxel value to an activity, a uniform cylindrical phantom of 185 MBq  $^{99m}\text{Tc}$  with dimensions identical to the NEMA IQ phantom was first GATE MC simulated and then reconstructed using our algorithm to derive a 3D look-up table containing voxel-by-voxel calibration factors.

### 2.5. Performance evaluation

In order to quantitatively assess the performance of the proposed collimation system, a set of phantoms were simulated. Various figure-of-merits (FOMs) such as geometric efficiency (sensitivity), spatial resolution, noise level, signal-to-noise ratio (SNR), and activity recovery coefficient (RC) were investigated, and also fairly compared to those of the current collimator. The data acquisition time for both of the collimators was kept the same (32 min).

#### 2.5.1. System sensitivity

The in-air system sensitivity was calculated for both collimators using a point source of 74 MBq  $^{99m}\text{Tc}$  located at a various source-to-collimator distances (SCDs) ranging from zero to 120 mm with an increment of 20 mm using the GATE. In addition, a high-count point source GATE simulation (148 MBq) was separately performed for measuring the sensitivity at 30 mm distance (typical ROR of the scanner). The sensitivity was calculated for 300 s data-acquisition period. All detected photons within a 20% energy-window centered at the photopeak have been considered for the sensitivity assessment. The system sensitivities were also scatter- and decay-corrected for the  $^{99m}\text{Tc}$  tracer (6 h half-life). To suppress the dependency of the sensitivity on angular position of the source at a given SCD for the slithole, we reported the mean sensitivity value over the FOV.

### 2.5.2. Tomographic resolution

The tomographic spatial resolution of the slithole, in terms of full-width-at-half-maximum (FWHM), was calculated for a dedicated phantom centered in the FOV of the camera using GATE MC simulations. The ROR was 30 mm. The phantom consists of five  $^{99m}\text{Tc}$  point sources (7.5 mm spacing and 18.5 MBq each) located within a NEMA IQ-like cylinder filled with water as depicted in Fig. 3. Sixteen equally-spaced spin projections over  $180^\circ$  span along with 16 equally-angled SPECT views through  $360^\circ$  span were acquired for a total 32 min scan time. The projection data were scatter-corrected and then the images were iteratively reconstructed using our dedicated OSEM framework with 3 full-iterations and 16 subsets. The image array was  $128 \times 128 \times 128$ , resulting in a voxel volume of  $(0.39 \text{ mm})^3$ .

Prior to reconstructing the above phantom, the developed algorithm was verified using a reference 3D noiseless Shepp-Logan phantom as a ground truth. Normalized squared error (NSE) was calculated as a metric indicating the reconstruction quality (or the accuracy) by measuring similarity between the true and the reconstructed image, using

$$\text{NSE}(\%) = \frac{\sum_{i=1}^N \sum_{j=1}^M (I_{ij} - \hat{I}_{ij})^2}{\sum_{i=1}^N \sum_{j=1}^M \hat{I}_{ij}^2} \times 100. \quad (2)$$

where  $I_{ij}$  is the reconstructed image,  $\hat{I}_{ij}$  is the original Shepp-Logan phantom,  $N$  and  $M$  are the image dimensions for a sample 2D slice. The phantom was analytically simulated using our forward projector with 16 spin angles and 16 SPECT angles, and was then reconstructed using our dedicated OSEM framework with 3 full-iterations and 16 subsets. The variable sensitivity was modeled during forward projecting, however, no attenuation or scatter was included in projection data generation.

For the parallel-hole collimator, the spatial resolution was measured using GATE MC simulation of a point source of 18.5 MBq  $^{99m}\text{Tc}$  at various distances followed by a standard OSEM reconstruction with 2 full-iterations and 16 subsets. Alternatively, the SPECT images were also reconstructed using a rotation-based resolution modeling OSEM algorithm [28]. The image array was  $128 \times 128 \times 128$ , resulting in a voxel volume of  $(0.39 \text{ mm})^3$ .

### 2.5.3. NEMA IQ phantom study

Evaluation of the image quality metrics, i.e., the noise characteristics, the SNR, and the RC was addressed by simulation of NEMA IQ phantom. The NEMA IQ phantom is a cylinder of 30 mm diameter and 50 mm length, and contains three parts: (1) five rods with different diameters (1, 2, 3, 4, and 5 mm) and 20 mm in length, (2) a

uniform part (15-mm in length), and (3) two cold (air-filled) cylinders [37]. The phantom was filled with 185 MBq  $^{99m}\text{Tc}$  tracer. Also, all imaging parameters were the ones chosen for the dedicated tomographic resolution phantom. To compare the performance of the slithole to that of the parallel-hole collimator, GATE simulation of the NEMA IQ phantom was repeated for the current parallel-hole collimator.

The coefficient of variation (COV) in the reconstructed image was reported as noise level in the drawn volume-of-interest (VOI) (a cylinder of 22.5 mm diameter and 10 mm length), using

$$\text{COV}(\%) = \frac{\sigma_U}{\text{mean}_U} \times 100. \quad (3)$$

where  $\sigma_U$  is the standard deviation of voxel values within the VOI and  $\text{mean}_U$  is the mean voxel value within the same VOI.

The quantity SNR was calculated for the largest rod (5 mm diameter) in hot region of the NEMA IQ phantom using

$$\text{SNR} = \frac{\text{mean}_H}{\sigma_{BG}}. \quad (4)$$

where  $\text{mean}_H$  is the mean of the voxel values in an outlined VOI (a cylinder of 5 mm diameter and 15 mm height centered at the 5 mm hot rod) and  $\sigma_{BG}$  is the standard deviation of the background. We considered  $\sigma_{BG}$  be identical to  $\sigma_U$ . To search for an optimal full-iteration number, the SNR was evaluated up to 7 full-iterations.

The activity recovery coefficient, or simply the RC, was quantized for each rod of the NEMA IQ phantom as follows

$$\text{RC} = \frac{\text{max}_H}{A_T}. \quad (5)$$

where  $\text{max}_H$  is the maximum voxel value in a VOI completely surrounding each rod (the diameter of each VOI is set to the corresponding rod diameter) and  $A_T$  is the true activity density of the corresponding rod. To mitigate the image noise effect, a high-statistics GATE MC simulation was performed. In addition, a small  $3 \times 3$  averaging window centered at the highest pixel value was considered, and the mean of the window was reported as the  $\text{max}_H$  value.

## 2.6. Experimental study and validation

The MC simulations were validated against the experiments for the parallel-hole collimator. The experiments were conducted with the imaging and the data-acquisition parameters as for the GATE simulations. A point source of  $^{99m}\text{Tc}$  located at various distances (zero, 40 mm, 80 mm, and 120 mm) was used for measuring the sensitivity.

## 3. Results

### 3.1. System sensitivity

The GATE MC simulated system sensitivity for the proposed collimator is plotted in Fig. 4. The slithole gives rise to a mean sensitivity of 285 cps/MBq ( $\sim 7.9$  times greater than the current  $\sim 36$  cps/MBq value) at a 30 mm ROR. Fig. 4 also compares the sensitivity of the slithole collimation with that of the current parallel-hole one. Fig. 5(a) and (b) illustrate the sensitivity profiles in two different directions (parallel and perpendicular to the slit aperture). The sensitivity values are also corrected for background, scatter, and  $^{99m}\text{Tc}$  half-life.

Fig. 6(a)–(c) show three orthogonal sections through the 3D sensitivity map. Although the map was determined for an  $11 \times 11 \times 11$  grid, it was resampled to match the image matrix ( $128 \times 128 \times 128$  matrix size) using a B-spline interpolation.

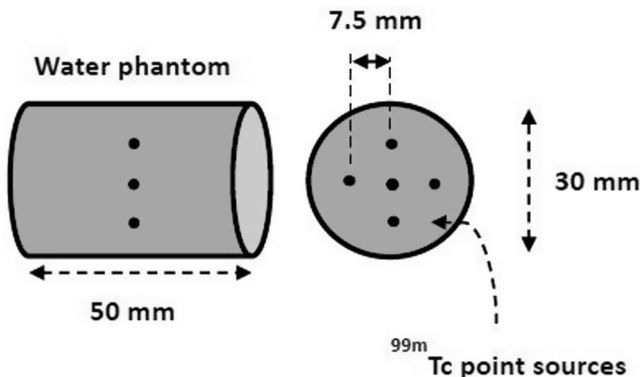
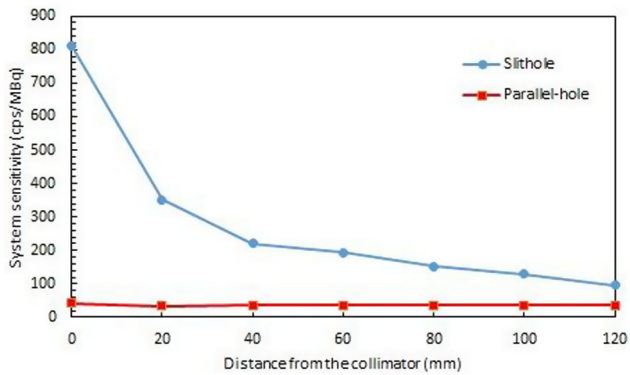


Fig. 3. Schematics of the dedicated five point sources phantom designed for assessing the system sensitivity. The source spacing is 7.5 mm and phantom is filled with water. The spatial resolution is averaged over these five point sources.



**Fig. 4.** Variation of system sensitivity of the slithole collimator across distance from the slit. Corresponding sensitivities for the current parallel-hole collimator are also shown.

### 3.2. Tomographic spatial resolution

The 3D Shepp-Logan phantom and its reconstruction using our dedicated algorithm are shown in Fig. 7. Referring to Fig. 7, an NSE of  $\sim 9\%$  for the 3D Shepp-Logan phantom image at 3 full-iterations confirms a good reconstruction quality. Tomographic resolution of both collimators (in terms of FWHM) as a function of ROR is depicted in Fig. 8. The average FWHM over the five point sources is reported as tomographic resolution for the slithole. At a typical

30 mm ROR (magnification factor of 1.5) spatial resolution of slit-hole, averaged over the five point sources, reaches 1.8 mm compared with a spatial resolution of 3.2 mm and 1.7 mm without and with resolution recovery, respectively, in the case of the parallel-hole collimator [30]. When tomographic resolution is reported for center of the FOV (the middle point source in Fig. 3), a spatial resolution of  $\sim 1.65$  mm is gained for the slithole collimator.

### 3.3. NEMA IQ phantom study

The original uniform part of the NEMA IQ phantom and its reconstruction for the parallel-hole and the slithole collimators are shown in Fig. 9. The COV of the uniform part of the NEMA IQ phantom image for slithole collimation reaches 4.79% compared with a COV of 8.41% for the current parallel-hole collimation (Fig. 9).

A sample slice of the original hot-rods part of the NEMA IQ phantom and its reconstruction for the parallel-hole and the slithole collimators are illustrated in Fig. 10. Dependency of the SNR on full-iteration number for both collimators is highlighted in Fig. 11. According to Fig. 11, optimal iteration number from a SNR point-of-view is 2 and 3 for the current parallel-hole and the slithole collimators, respectively. For the parallel-hole collimation data, we utilized an OSEM algorithm with 16 subsets. In addition, Fig. 12 plots variation of the RC against rod size for both collimation systems. The slithole offers an RC of  $\sim 0.83$  for the largest rod (Fig. 12).

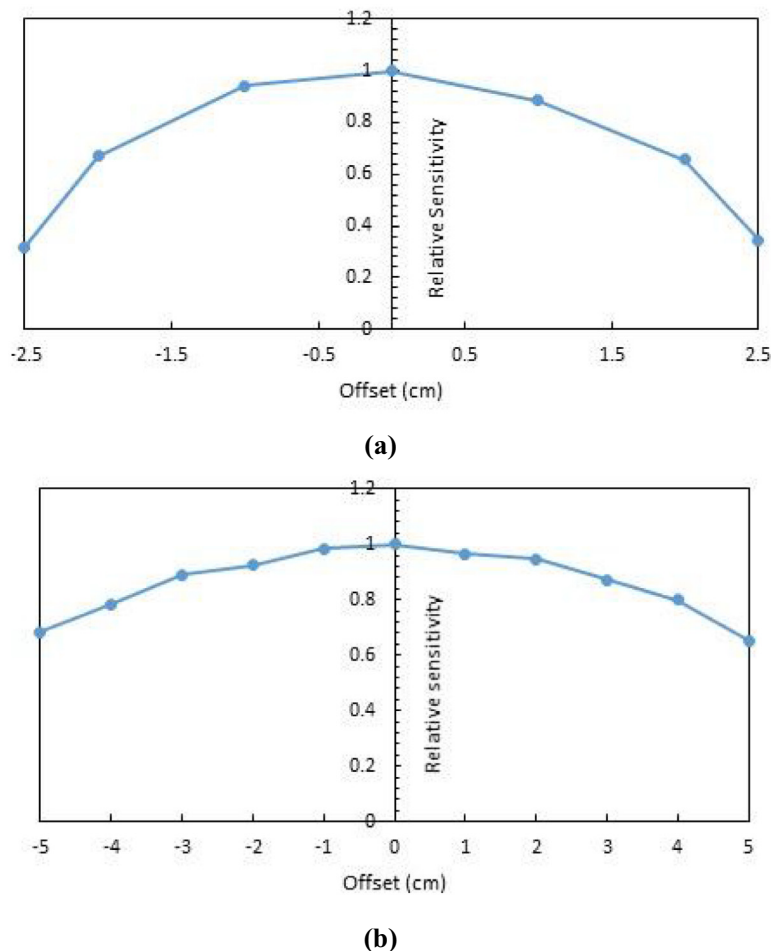


**Fig. 5.** Normalized sensitivity profiles across two different directions: (a) perpendicular to the slit and (b) parallel to the slit.

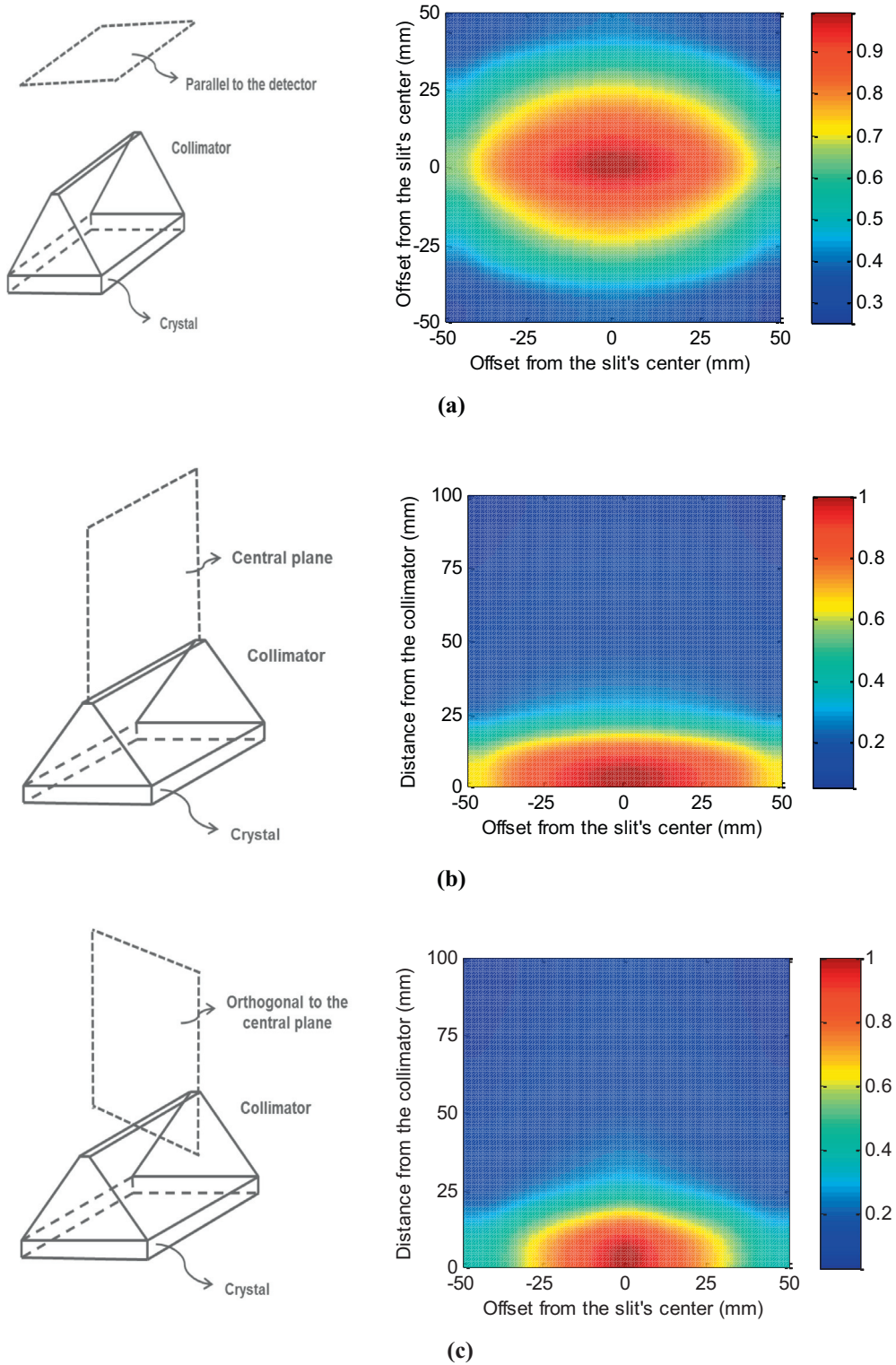


**Fig. 6.** The 3D sensitivity map: (a) sensitivity variation in a plane parallel to the detector, (b) sensitivity variation in the central plane of the collimator, and (c) sensitivity variation in a plane orthogonal to the central plane.

3.4. Validation of the GATE simulation

Fig. 13 provides a comparison between the decay-corrected MC simulated and the experimental system sensitivity for the parallel-hole collimator. The GATE simulations and the experiments are in good agreement with a maximum ~11% difference at 120 mm distance.

4. Discussion

As expected, a great improvement in the system sensitivity was obtained originating from the enlarged solid angle of photon acceptance afforded by the slithole. Compared with a constant sensitivity of a parallel-hole collimator in its FOV, the sensitivity of the slithole is decaying with approximately  $\frac{1}{d(d+F)}$  trend, where the  $d$  is

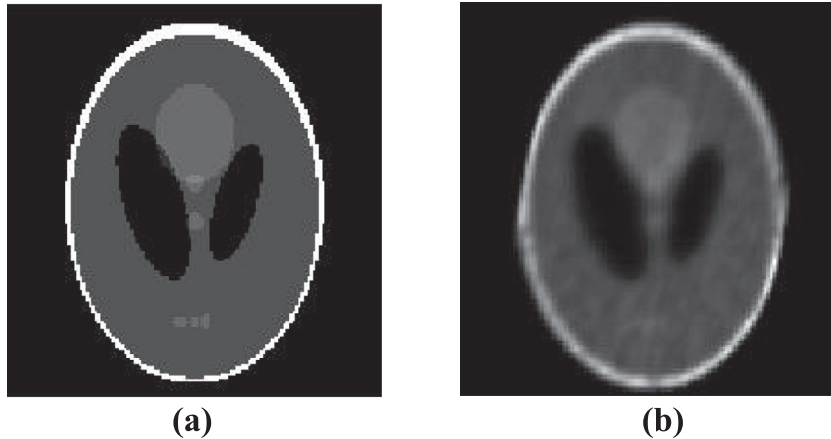


**Fig. 7.** (a) A sample slice of the 3D noise-free Shepp-Logan phantom and (b) its reconstruction using the dedicated OSEM framework. The image matrix is  $128 \times 128$  resulting in 0.39 mm pixel size.

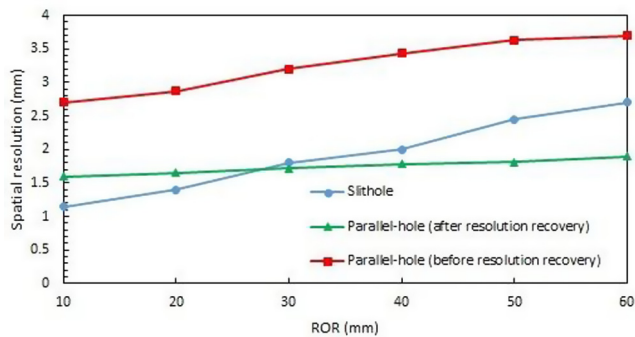


**Fig. 8.** Comparison of tomographic resolution for the slithole collimator with the current parallel-hole one (without and with resolution recovery) against ROR.

the distance from the collimator in the central plane and  $F$  is the focal length of the collimator, as previously published by Zeng et al. [24]. The sensitivity of the slithole collimator also varies with the angle between the line connecting the point-of-interest to the slit's center and the central plane of the collimator (Fig. 5(a)). For those points located in a plane orthogonal to the central plane, the behavior approximately follows  $\cos \theta$  where  $\theta$  is the aforementioned angle. It is also interesting to characterize the sensitivity across those points which are parallel to the slit (Fig. 5(b)). Moving

towards to both ends of the slit, the sensitivity is dropped mainly due to a reduction in the solid angle (Fig. 6(a) and (b)). To sum up, the overall weighting factor would be  $\frac{g(s) \times \cos \theta}{d(d+F)}$  for all points within the FOV. The  $g(s)$  term accounts for dropping the system sensitivity in directions parallel to the slit aperture, as shown in Fig. 6(b).

As can be read from the curve in Fig. 8, the spatial resolution of the slithole deteriorates as distance from the slit increases. For close distances (up to 30 mm) the slithole outperforms the parallel-hole collimator even if a resolution modeling method is applied to the parallel-hole collimation data. The spatial resolution of the slithole worsens towards the edge of the FOV (from 1.65 mm at the center to 1.8 mm at the FOV edge). The origin of such a non-uniformity in the spatial resolution of the slithole within the FOV is primarily inter-crystal scatter and penetration phenomena which occurred in our pixelated crystal for oblique planar projections. For the designed collimator, this oblique angle reach up to  $\sim 30^\circ$  (half the opening angle). It is worth noting that we embedded the five point sources in a water phantom to assess the spatial resolution in presence of a scattering medium as well as to evaluate the ability of the scatter correction strategy.

The reduction in the image noise level (from 8.41% to 4.79%) is due to the improvement in the system sensitivity. Compared to  $\sim 7.9$  times higher system sensitivity, the noise level is reduced by a factor of  $\sim 1.75$ . The improvement in system sensitivity is solely dependent on the system geometry (i.e., it is machine-dependent),

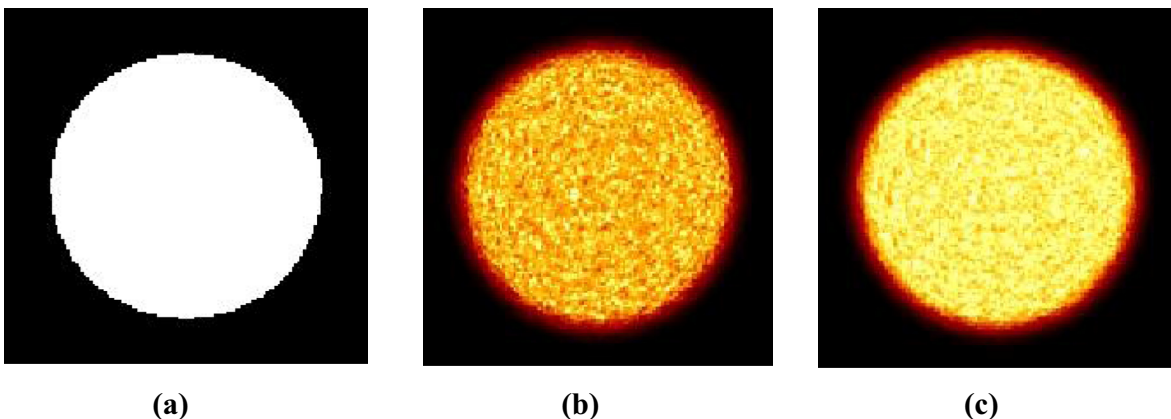


**Fig. 9.** (a) A sample slice of the original uniform part of the NEMA IQ phantom, (b) its reconstruction for the current parallel-hole collimator, (c) its reconstruction for the slithole collimator.

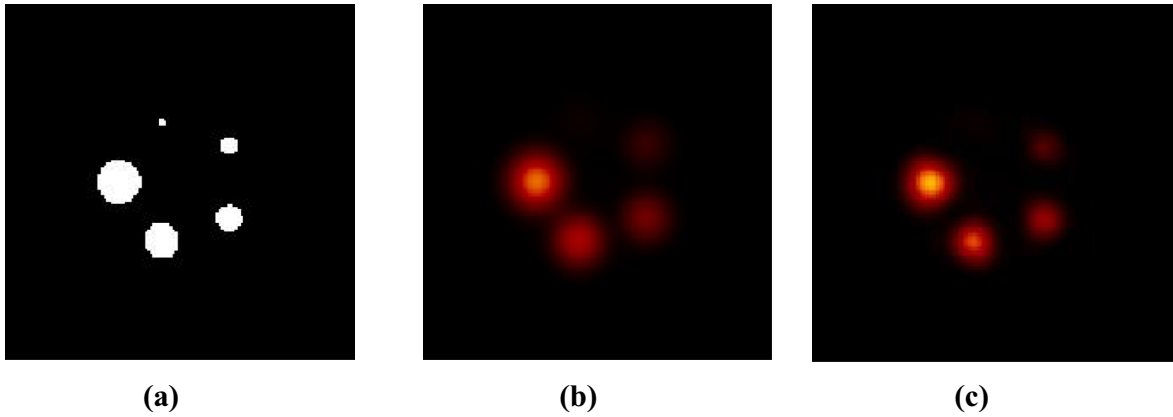


**Fig. 10.** (a) A sample slice of the original hot-rod part of the NEMA IQ phantom, (b) its reconstruction for the current parallel-hole collimator, (c) its reconstruction for the slithole collimator.

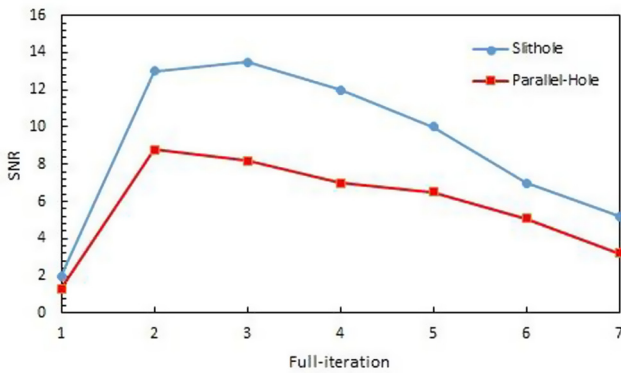


**Fig. 11.** SNR versus full-iteration number for the parallel-hole and the slithole collimated HiReSPECT scanner. The SNR values are calculated for the largest rod in the hot region of the NEMA IQ phantom.

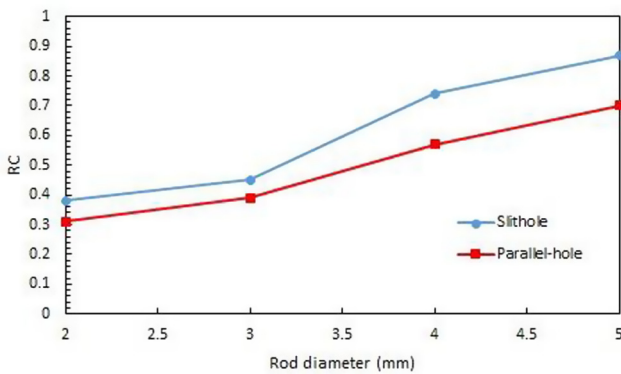


**Fig. 12.** Dependency of RC value on rod diameter in the NEMA IQ phantom reconstruction for the parallel-hole and the slithole collimated HiReSPECT scanner.

while other factors such as the imaging parameters as well as the reconstruction algorithm settings also contribute to the noise reduction (i.e., it is image-dependent). For a 32 min total imaging time, there are 64 projections for the parallel-hole collimator while 265 projections (16 spin angles  $\times$  16 SPECT angles) exist in the case of slithole collimation. By increasing the scan time, a bigger reduction in the image noise level would be observed.

As demonstrated in Fig. 11, the SNR has its maximum value at iteration number of 2 and 3 for the parallel-hole and the slithole collimators, respectively. Beyond these iteration numbers, the

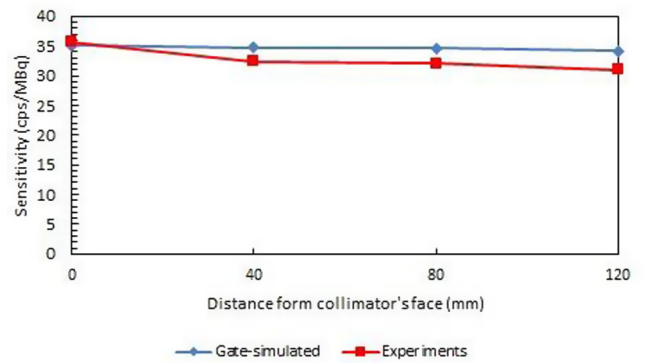


**Fig. 13.** Comparison of the MC simulated with the measured system sensitivity across distance for the parallel-hole collimation.

SNR drops because the noise propagation dominates at higher iterations. Therefore, these iteration numbers can be considered as the optimal iteration numbers for such a complicated phantom. Due to the higher detection efficiency of the slithole than that of the parallel-hole, a higher SNR up to a factor of 1.53 is observed. In assessing the SNR for both collimators, the largest rod (diameter of 5 mm) was chosen, because it includes more image voxels compared with the other rods and therefore the SNR is more statistically reliable. As for the noise level, the SNR also depends on the imaging parameters and the reconstruction settings.

The RC versus rod diameter curve owns a unique feature by combining the image contrast with the spatial resolution. In nuclear medicine, the image contrast is influenced by the partial volume effect (PVE) and therefore because of the PVE, recovery of the true activity in a SPECT scan depends on the lesion size. In other words, the finite spatial resolution of the camera contributes to the RC. The PVE spreads out the activity around the object, and leads to an underestimation of the activity in the case of hot lesions. For the same activity density, a larger lesion size attributes a higher RC. According to our results for both collimators, the RC improves as the rod diameter increases (Fig. 12). The slithole shows an advantage in RC for all hot lesion sizes over the current parallel-hole collimator, mainly due to its higher spatial resolution. The RCs are calculated at 2 and 3 full-iterations for the parallel-hole and the slithole, respectively.

Though it is true that the combination of a larger focal length as well as a wider detection area always leads to superior image quality characteristics, the designed slithole collimation can still be considered as the optimal solution fulfilling our needs. As

mentioned previously, we looked for a slithole geometry that suits SPECT imaging with the current HiReSPECT configuration considering all limitations.

## 5. Conclusion

This research reports results of a novel high-sensitivity collimation system for small animal SPECT. The geometry of the newly proposed collimator as well as the imaging parameter settings were specified for the HiReSPECT scanner. Based upon our findings, one can conclude that the slithole collimation provides a better balance between the competing tomographic resolution and the system sensitivity compared with a parallel-hole collimator. When using the slithole collimation, an average 7.9 times increase in the system sensitivity (at a 30 mm ROR) is gained without remarkably compromising spatial resolution. Furthermore, the slithole takes advantage of a much lower weight than its parallel-hole alternative. This feature enables use of lower-cost stepper motors as well as less demands for mechanical calibration; all make the slithole collimated HiReSPECT camera favorable for application in SPECT molecular imaging.

The slithole, however, needs optimizations particularly for its edge. Although knife-edge collimators are simple and common in small animal SPECT, they consequently result in a high edge penetration specially in high-energy (for example,  $^{131}\text{I}$ ) SPECT imaging. In the slithole collimator in which there is long slit aperture, the edge penetration plays an undeniable role. To this end, designing a keel-edge slithole (rather than the conventional knife-edge one) can potentially overcome the problem. Therefore, we are searching for an optimum keel (channel) height for the slithole in our future study. Moreover, possibility of designing a multi-slithole collimation system is a matter of ongoing research.

## Acknowledgments

This work was supported by Research Center for Molecular and Cellular Imaging (RCMCI), Tehran University of Medical Science under grant No. 29885.

## References

- [1] Kemp RAD et al. Small-animal molecular imaging methods. *J Nucl Med* 2010;51:185–32S.
- [2] Zaidi H. Quantitative analysis in nuclear medicine imaging. New York: Springer Science + Business Media, Inc.; 2006.
- [3] Zaidi H. Molecular imaging of small animals: instrumentation and applications. New York: Springer; 2014.
- [4] Zaidi H. Quantitative analysis in nuclear medicine imaging. Singapore: Springer; 2006.
- [5] Zaidi H. Recent developments and future trends in nuclear medicine instrumentation. *Z Med Phys* 2006;16:5–17.
- [6] Meikle SR. Small animal SPECT and its place in matrix of molecular imaging technologies. *Phys Med Biol* 2005;50:45–61.
- [7] Madsen MT. Recent advances in SPECT imaging. *J Nucl Med* 2007;48:661–73.
- [8] Kupinski MA, Barrett HH. Small-animal SPECT imaging. New York: Springer Science + Business Media, Inc.; 2005.
- [9] Rahmim A, Zaidi H. PET versus SPECT: strength, limitations and challenges. *Nucl Med Commun* 2008;29:193–207.
- [10] Audenhaege KV et al. Review of SPECT collimator selection, optimization, and fabrication for clinical and preclinical imaging. *Med Phys* 2015;42:4927061.
- [11] Mauderli W et al. A computerized rotating laminar radionuclide camera. *J Nucl Med* 1979;20:341–4.
- [12] Chiu MY et al. Three-dimensional reconstruction from planar projections. *J Opt Soc Am* 1980;70:070755.
- [13] Gindi GR et al. Imaging with rotating slit apertures and rotating collimators. *Med Phys* 1982;9:324–39.
- [14] Webb S. Monte Carlo modeling of the performance of a rotating slit-collimator for improved planar gamma-camera imaging. *Phys Med Biol* 1992;37:1095–108.
- [15] Webb S et al. Geometric efficiency of a rotating slit-collimator for improved planar gamma-camera imaging. *Phys Med Biol* 1993;38:627–38.
- [16] Lodge MA et al. A prototype rotating slit collimator for single photon emission computed tomography. *IEEE Trans Med Imaging* 1996;15:500–11.
- [17] Lodge MA et al. The experimental evaluation of a rotating slit collimator for planar gamma camera imaging". *Phys Med Biol* 1995;40:427–48.
- [18] Gagnon D et al. Design considerations for a new solid-state gamma camera: solstice. *IEEE Nucl Sci Med Imaging Conf* 2001;2:1156–60.
- [19] Dehestani N et al. Comparative assessment of rotating slit and parallel hole collimator performance in GE DST-Xli gamma camera: a Monte Carlo study. *Proc IFMBE Conf* 2008;22:1062–5.
- [20] Holen R et al. Comparing planar image quality of rotating slit and parallel Hole collimation: influence of system modeling. *Phys Med Biol* 2008;53:1989–2002.
- [21] Holen RV, Staelens S, Vandenberghe S. Tomographic image quality of rotating slit versus parallel hole-collimated SPECT. *Phys Med Biol* 2011;56:7205–22.
- [22] Boisson F et al. Characterization of a rotating slit collimator system dedicated to small animal imaging. *Phys Med Biol* 2011;56:1471–85.
- [23] Boisson F et al. Assessment of a fast generated analytical matrix for rotating slit collimation iterative reconstruction: a possible method to optimize the collimation profile. *Phys Med Biol* 2015;60:2403–19.
- [24] Zeng GL, Gagnon D. CdZnTe strip detector SPECT imaging with a slit collimator. *Phys Med Biol* 2004;49:2257–71.
- [25] Moji V et al. Performance evaluation of a newly developed high-resolution, dual-head animal SPECT system based on the NEMA NU1-2007 standard. *J Appl Clin Med* 2014;15:267–87.
- [26] Sajedi S et al. Design and development of a high resolution animal SPECT scanner dedicated for rat and mouse imaging. *Nucl Instr Meth Phys Res A* 2014;741:169–76.
- [27] Pashazadeh AM et al. Experimental evaluation of the performance of HiReSPECT scanner: a high-resolution SPECT system for small animal imaging. *Front Biomed Technol* 2014;1:222–7.
- [28] Zeraatkar N et al. Resolution-recovery-embedded image reconstruction for a high resolution animal SPECT system. *Phys Med* 2014;30:774–81.
- [29] Mahani H et al. Monte Carlo optimization of crystal configuration for pixelated molecular SPECT scanners. *Nucl Instr Meth Phys Res A* 2017;844:1–6.
- [30] Mahani H et al. Collimator-detector response compensation in molecular SPECT reconstruction using STIR framework. *Iran J Nucl Med* 2017;25:26–34.
- [31] Shepp LA, Vardi Y. Maximum likelihood reconstruction for emission tomography. *IEEE Trans Med Imaging* 1982;1:113–22.
- [32] Mahani H et al. How gamma camera's head-tilts affect image quality of a nuclear scintigram? *Front Biomed Technol* 2014;1:265–70.
- [33] Santin G et al. GATE: a Geant4-based simulation platform for PET and SPECT integrating movement and time management. *IEEE Trans Med Imaging* 2003;50:1516–21.
- [34] Jan S et al. GATE V6: a major enhancement of the GATE simulation platform enabling modelling of CT and radiotherapy. *Phys Med Biol* 2011;56:881–901.
- [35] Sakellios N et al. GATE simulations for small animal SPECT/PET using voxelized phantoms and rotating detectors. *IEEE Nucl Sci Symp Conf Rec* 2006:2000–3.
- [36] Jaszczak RJ et al. Improved SPECT quantification using compensation for scattered photons. *J Nucl Med* 1984;25:893–900.
- [37] NEMA. Performance measurements of small animal positron emission tomographs (PETs). NEMA NU-4-2008. Rosslyn, VA: National Electrical Manufacturers Association; 2008.